

A Novel Mixed Valent Chromium-Layered Oxide with Peculiar Magnetic Properties: $\text{Sr}_{4.5}\text{Cr}_{2.5}\text{O}_9$

D. Pelloquin, A. Wahl, A. C. Masset, A. Maignan, C. Michel, and B. Raveau

Laboratoire CRISMAT, UMR 6508, ISMRA et Université de Caen, 6, Boulevard du Maréchal Juin, F-14050 Caen Cedex, France

Received March 21, 2000; in revised form June 1, 2000; accepted June 16, 2000; published online September 30, 2000

A new mixed valent chromium-layered oxide, $\text{Sr}_{4.5}\text{Cr}_{2.5}\text{O}_9$, with a structure closely related to the “0201–1201” structure of the superconducting cuprate $\text{TlBa}_{2-x}\text{La}_{2+x}\text{Cu}_2\text{O}_9$, has been synthesized at normal pressure. This orthorhombic phase ($a = 10.7959(2)$ Å, $b = 5.4012(1)$ Å, and $c = 30.0755(6)$ Å) consists of the regular intergrowth of $[\text{Sr}_2\text{CrO}_4]^{0201}$ blocks and $[(\text{Sr}_{0.5}\text{Cr}_{0.5})\text{Sr}_2\text{CrO}_5]^{1201}$ blocks. It differs from the thallium cuprate by the 1:1 ordering of Sr and Cr species within the intermediate layer of the “1201” block, so that at this level CrO_4 tetrahedra, containing Cr^{6+} species, are obtained. Moreover, at the boundary between the “1201” and “0201” blocks, CrO_6 octahedra alternate with CrO_5 pyramids, both occupied by Cr^{3+} species. The magnetic measurements show an original metamagnetic transition from an antiferromagnetic to a weak ferromagnetic state. These properties are interpreted in terms of strong intralayer and weak interlayer magnetic couplings between Cr^{3+} species through a superexchange mechanism. © 2000 Academic Press

INTRODUCTION

Layered oxides related to the Ruddlesden and Popper structures (1) form a large family with attractive physical properties as shown for the layered cuprates that are exceptional superconductors (2) and manganites for which colossal magnetoresistance properties were observed (3). Such intergrowths were also observed for iron and cobalt oxides as exemplified by the series $M\text{Sr}_4\text{Fe}_2\text{O}_9$ with $M = \text{Tl}, \text{Pb}, \text{Hg}, \text{Pr}$ (4–7) and by the oxides $\text{Bi}_{0.5}\text{Cd}_{0.3}\text{Sr}_2\text{Co}_{1.2}\text{O}_{5-\delta}$ (8), $\text{Bi}_2\text{Sr}_2\text{CoO}_{6+\delta}$ (9), and $\text{Bi}_{1-x}\text{Sr}_{3+x}\text{CoO}_{6-\delta}$ (10). In contrast to these first series of transition elements, chromium does not show a great ability to form such layered oxides despite the existence of the perovskite structure for LnCrO_3 (11). Nevertheless, the oxides of the LnCaCrO_4 series (12), with a distorted K_2NiF_4 -type structure, are of high interest since they exhibit particular magnetic properties characterized by a progressive transition from a 2D magnetic behavior toward a 3D one as the size of the Ln^{3+} cation decreases (13). Moreover, the synthesis of $\text{Ca}_{1+x}\text{Y}_{1-x}\text{CrO}_4$ related also to K_2NiF_4 structure, where chromium exhibits a $\text{Cr}(\text{III})$ –

$\text{Cr}(\text{IV})$ mixed valence (14), suggests the possibility of generating other new members with a closely related structure in such systems by controlling the various oxidation states of chromium, $\text{Cr}(\text{VI})$, $\text{Cr}(\text{V})$, $\text{Cr}(\text{IV})$, and $\text{Cr}(\text{III})$. Curiously the Sr_2CrO_4 phase does not exhibit the K_2NiF_4 structure under normal conditions of synthesis but a β - K_2SO_4 -type structure (15), where $\text{Cr}(\text{IV})$ is in tetrahedral coordination, in contrast to rutile CrO_2 , where it is octahedral (16). In order to understand this particular behavior, we have investigated the system $\text{Sr}–\text{Cr}–\text{O}$, bearing in mind that the stability of the various oxidation states in such a system may strongly depend on the synthesis conditions. We report herein a new layered oxide, $\text{Sr}_{4.5}\text{Cr}_{2.5}\text{O}_9$, derived from the “0201–1201”-type structure previously observed in the superconducting cuprate $\text{TlBa}_{2-x}\text{La}_{2+x}\text{Cu}_2\text{O}_9$ (17), but with different chromium coordinations and valencies forming tetrahedra occupied by Cr^{6+} and mixed octahedra–pyramids occupied by Cr^{3+} . The magnetic study of this new oxide shows an original metamagnetic transition at low temperature from an antiferromagnetic state to a weak ferromagnetic state by applying a magnetic field. We believe that such properties can be explained by the existence of strong intralayer and weak interlayer couplings between the Cr^{3+} species through a superexchange mechanism.

EXPERIMENTAL

The system $\text{Sr}–\text{Cr}–\text{O}$ has been scanned considering non-stoichiometric K_2NiF_4 -type compositions, namely $\text{Sr}_{2-x}\text{CrO}_{4-y}$. All samples were prepared by solid state reaction from SrO , SrO_2 , and Cr_2O_3 precursors. SrO oxide was initially prepared by decomposing SrO_2 peroxide at 1100°C . To avoid the contamination from carbonate and hydroxide groups and to control the oxygen content, the precursors were weighted and intimately ground in a dry box. Next the mixtures were pressed into bars, placed in an alumina finger, and sealed in an evacuated quartz ampule. Then the different samples were heated to 1200°C , at $200^\circ\text{C}\cdot\text{h}^{-1}$, kept at this temperature for 24 h, and cooled to room temperature.

Structural characterizations were first carried out using transmission electron microscopy techniques. The different electron diffraction (ED) patterns used to build the reciprocal space were recorded with a JEOL 200CX electron microscope fitted with an eucentric goniometer ($\pm 60^\circ$). Afterward, the high-resolution electron microscopy (HREM) was carried out with a TOPCON 002B operating at 200 kV and having a point resolution of 1.8 Å. The two microscopes are equipped with EDX analyzers. Then the structural model defined from these observations was refined from X-ray powder diffraction (XRPD) data collected with a Philips vertical diffractometer (CuK α radiation) in the range $5^\circ \leq 2\theta \leq 110^\circ$ by increments of 0.02° (2θ). The structural calculations were performed by Rietveld profile analysis with the Fullprof software (version 3.7) (18). HREM image calculations were carried out with the Mac-Tempas multislice program.

The oxygen content was determined by chemical analysis using redox titration while density measurements were carried out at $T = 25^\circ\text{C}$ with a picnometer working with carbon tetrachlorure solution.

DC magnetization measurements in the range 5–400 K were performed using a SQUID Quantum Design magnetometer (ZFC method) and at high temperature (300–800 K) using Faraday method with an applied field of 3 kG.

RESULTS AND DISCUSSION

For the above conditions of synthesis, a new phase was identified for the nominal composition $\text{Sr}_{1.8}\text{CrO}_{3.6}$ (i.e., the molar ratios 1.5 SrO, 0.3 SrO₂, and 0.5 Cr₂O₃). The XRPD pattern of the latter suggests close relationships with the K₂NiF₄ structure. Nevertheless the structural study, combining electron microscopy and X-ray diffraction, showed that it is a more complex structure resulting to a regular intergrowth mechanism.

I. EDH and HREM Study: Evidence for a “0201–1201” Structure

The reciprocal space for numerous crystallites was reconstructed by tilting around the crystallographic axes. This first analysis shows that this phase is related to a perovskite-layered structure. The system of intense reflections evidences an orthorhombic cell with $a \approx b \approx a_p\sqrt{2}$ (a_p is the parameter of the cubic perovskite-type structure) and $c \approx 30$ Å while the main condition limiting the reflections ($hkl, k + l = 2n$) involves an A-type lattice. These ED patterns (Fig. 1) systematically exhibit extra weak reflections, which indicates a doubling of the a parameter. So the actual cell is orthorhombic with $a = 2a_p\sqrt{2} \approx 10.8$ Å, $b = a_p\sqrt{2} \approx 5.4$ Å, $c \approx 30$ Å, $hkl, k + l = 2n$, and $h0l, h = 2n$, com-

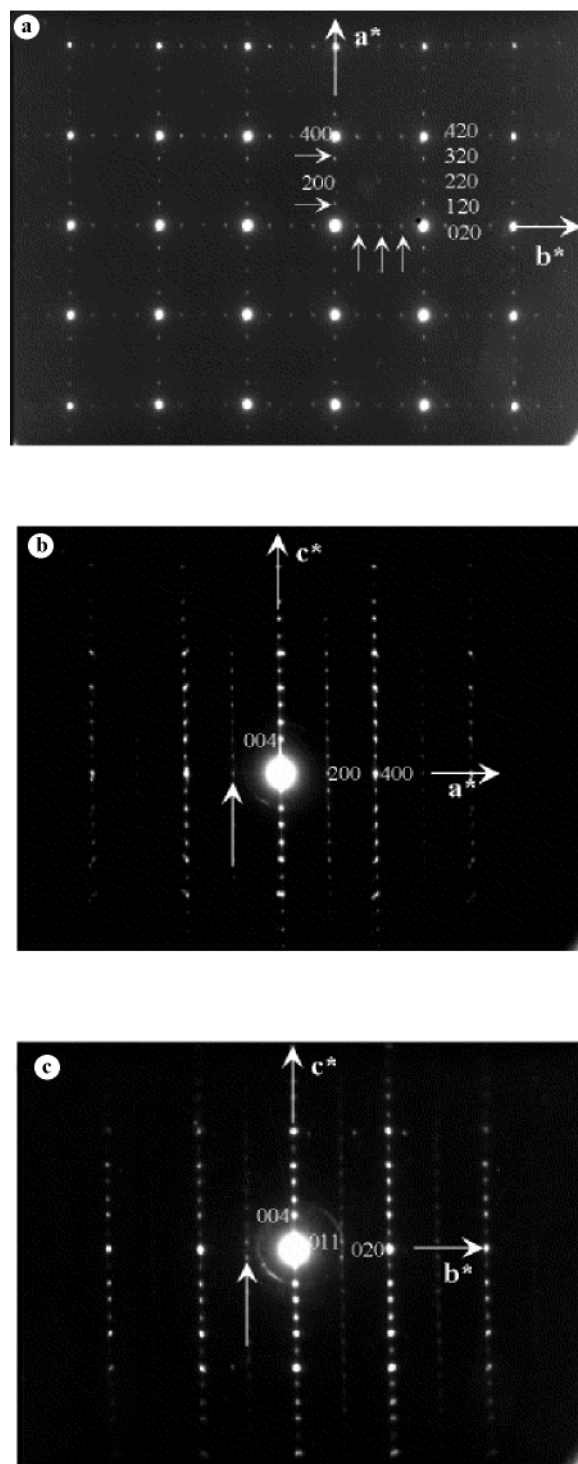


FIG. 1. Experimental ED patterns oriented along the (a) [001], (b) [010], and (c) [100] directions. The patterns are indexed in the supercell $2a_p\sqrt{2} \times a_p\sqrt{2} \times c$.

patible with the space groups $Amam$, $A2_1am$, and $A2_122$. Moreover twinning phenomena are often observed, which result from the A-type distortion of the pseudo-tetragonal subcell. This is clearly illustrated in the [001] ED pattern

(Fig. 1a) where complex extra spots (white arrows) ascribed to 90° oriented domains and double diffraction effects are observed. The numerous EDX analyses lead to an average Sr/Cr ratio equal to 1.8, in agreement with the nominal composition. Taking into account the size of the primitive cell, the space group deduced from ED observations, and the experimental density, $5.07(5) \text{ g/cm}^3$, a molar mass $M = 668 \text{ g}$ is found. On the basis of this M value, the cationic composition “ $\text{Sr}_{4.5}\text{Cr}_{2.5}$ ” could be proposed while the global oxygen content, determined by usual redox titration, is found to be close to 8.9(1).

In order to identify the stacking mode and the nature of different layers running along \vec{c} , a HREM study was carried out. Two characteristic orientations, namely $[2\bar{1}0]$ and $[100]$ type, were especially selected. The first one is shown in Fig. 2, with the corresponding ED pattern in inset, where the zones of high electron density are imaged as dark dots. This image shows clearly double and triple rows of staggered dark dots regularly separated by a row of smaller dark dots along the \vec{c} axis. Such adjacent rows of staggered dots, spaced by 3.8 \AA , correspond to contrasts typical of $[\text{AO}]_\infty$ layers. So these blocks of dark dots may be correlated to double and triple adjacent $[\text{SrO}]$ layers respectively, whereas the single row of smaller dark dots, interleaved between one double and one triple row of dark dots, can be correlated to a chromium layer. Such a stacking mode would lead to the following sequence: $[\text{CrO}_2]_\infty - [\text{SrO}]_\infty - [\text{SrO}]_\infty - [\text{CrO}_2]_\infty - [\text{SrO}]_\infty - [\text{SrO}]_\infty - [\text{SrO}]_\infty - [\text{SrO}]_\infty - [\text{CrO}_2]_\infty$. Moreover it would suggest that this oxide corresponds to the

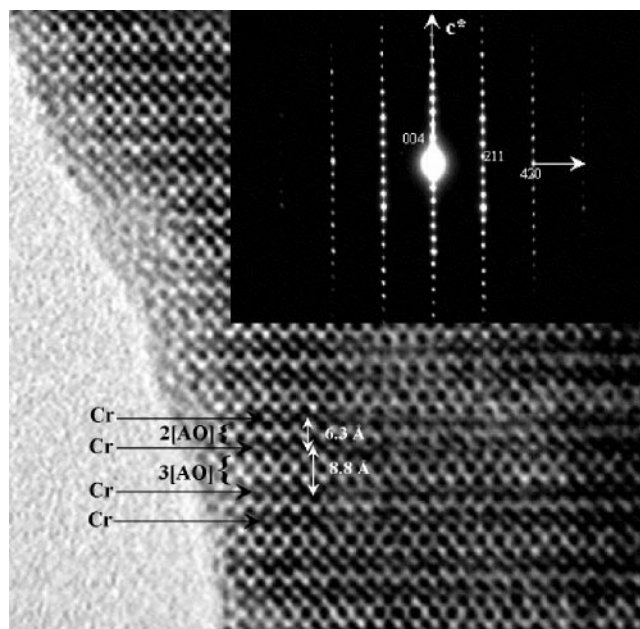


FIG. 2. Experimental HREM image and corresponding ED pattern (inset) recorded along the $[2\bar{1}0]$ direction. Dark dots are correlated to cation rows.

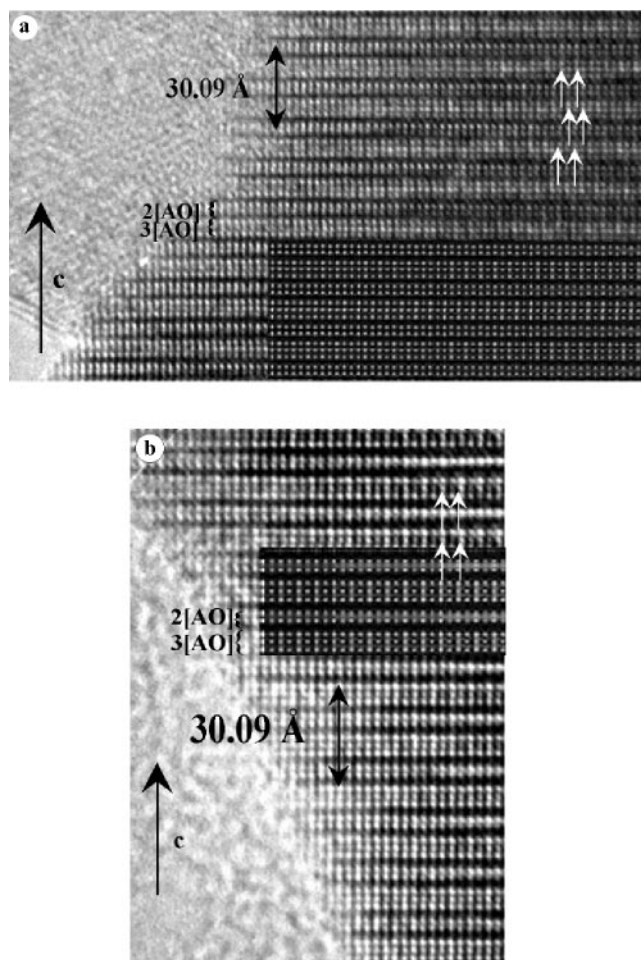


FIG. 3. Experimental HREM images recorded along the (a) $[100]$ and (b) $[010]$ directions. Bright and gray dots are correlated to strontium and chromium rows, respectively. The corresponding simulated images are inserted.

intergrowth of single octahedral layers with double and triple SrO layers, i. e., to the intergrowth of “0201” (Sr_2CrO_4) and “1201” ($\text{SrSr}_2\text{CrO}_5$) structures. Nevertheless, such a hypothesis implies the formula $\text{Sr}_5\text{Cr}_2\text{O}_9$ significantly different from the actual one, $\text{Sr}_{4.5}\text{Cr}_{2.5}\text{O}_{8.9}$. The existence of extra spots along $[010]$ - and $[100]$ -oriented ED patterns (white arrows in Figs. 1b and 1c), implying a supercell “ $2a_p\sqrt{2} \times a_p\sqrt{2} \times c$ ” with respect to the theoretical 0201–1201 structure ($a_p \times a_p \times c$), suggests that chromium may partly replace strontium in an ordered manner. The HREM images recorded along $[100]$ and $[010]$, with highlighted cationic positions (Fig. 3), confirm this viewpoint. The $[100]$ HREM image (Fig. 3a) shows on the edge of the crystal successively three adjacent rows and two adjacent rows of bright dots separated by single rows of small gray dots, which correspond to a triple $[\text{AO}]_\infty$ layer, a single $[\text{CrO}_2]_\infty$ layer, and a double $[\text{AO}]_\infty$ layer, respectively. Such a stacking mode is consistent with the previous $[2\bar{1}0]$

HREM observations. Nevertheless this contrast type (bright dots spaced by 2.7 Å) is modified in the thicker zone in triple $[AO]_{\infty}$ layers, especially at the level of the intermediate layer, one bright dot (white arrow) alternating with one gray dot. Moreover this ordered contrast is shifted by $a_p/\sqrt{2}$ from one triple layer to the next, in agreement with the shifted position of extra spots with respect to fundamental reflections (white arrow in Fig. 1c) in the corresponding ED pattern. The $[010]$ -oriented image (Fig. 3b) exhibits a similar alternation of one bright dot and one gray dot at the level of triple $[AO]_{\infty}$ layers, but contrary to the latter no shift of this ordered contrast is observed (white arrows) between two successive triple $[AO]_{\infty}$ layers. Such an observation is also consistent with the aligned position of extra spots with respect to fundamental reflections in the $[010]$ ED pattern (white arrows in Fig. 1b).

Taking into account the actual chemical composition deduced from analyses, namely $Sr_{4.5}Cr_{2.5}O_{8.9}$, these ordered contrasts can be ascribed to a 1:1 ordering between strontium and chromium species within the triple $[AO]_{\infty}$ layers, at the level of the intermediate layer, so that the actual stacking sequence along \vec{c} should be



II. XRPD Study: Structural Model

In order to check this stacking sequence determined by HREM, structure calculations were performed using XRPD data. The whole XRPD pattern of this phase was indexed in an orthorhombic cell with $a = 10.7959(2)$ Å, $b = 5.4012(1)$ Å, and $c = 30.0755(6)$ Å. The starting positions for those calculations were based on the atomic positions found out for the “0201–1201” structure of $TlBa_{2-x}La_{2+x}Cu_2O_9$ [17] (space group $I4/mmm$), but taking into account the 1:1 ordering of Sr and Cr in the $[(Sr_{0.5}Cr_{0.5})O]$ layer, leading to a supercell. The calculations were first carried out in the space group $Amam$, using a global B factor of 1 \AA^2 for oxygen atoms in order to avoid a too high number of variable parameters. The impurity phase Sr_2CrO_4 (15) was introduced in the calculations. The refinements of atomic parameters using this space group did not make it possible to lower the R_i factor below 0.104. Refinements were then carried out in the noncentrosymmetric space group $A2_1am$. Different attempts of refinement did not change significantly the positions of the metallic atoms, but evidenced a splitting of the oxygen sites O(1), O(2), and O(4) surrounding Cr(1) at the level of the triple $[AO]_{\infty}$ layer. Thus, the reliability factors were lowered to $R_i = 0.077$, $R_p = 0.113$, and $R_{wp} = 0.149$ for the final atomic coordinates listed in Table 1. The observed and calculated XRPD

TABLE 1

Atom	Site	x	y	z	$B(\text{\AA}^2)$	n
Sr(1)	4a	0.0 ^a	0.0 ^a	0.0	1.4(2) ^b	1
Sr(2)	8b	0.0 ^a	0.5 ^a	0.0841(2)	0.3(2)	1
Sr(3)	8b	0.25 ^a	0.0 ^a	0.0844(2)	0.9(2)	1
Sr(4)	8b	0.0 ^a	0.5 ^a	0.2053(2)	0.4(2)	1
Sr(5)	8b	0.25 ^a	0.0 ^a	0.2048(2)	0.8(2)	1
Cr(1)	4a	0.236(2)	0.473(2)	0.0	1.4(2) ^b	1
Cr(2)	8b	0.0 ^a	0.0 ^a	0.1457(4)	0.6(4)	1
Cr(3)	8b	0.25 ^a	0.5 ^a	0.1522(4)	1.2(4)	1
O(1)	4a	0.050(4)	0.5 ^a	0.0	0.7(2) ^c	1
O(2)	4a	0.25 ^a	0.100(4)	0.0	0.7(2) ^c	1
O(3)	8b	0.0 ^a	0.0 ^a	0.075(1)	0.7(2) ^c	1
O(4)	8b	0.277(4)	0.555(4)	0.0503(9)	0.7(2) ^c	1
O(5)	8b	0.0 ^a	0.0 ^a	0.213(1)	0.7(2) ^c	1
O(6)	8b	0.25 ^a	0.5 ^a	0.215(1)	0.7(2) ^c	1
O(7)	8b	0.125 ^a	0.25 ^a	0.153(2)	0.7(2) ^c	1
O(8)	8b	0.125 ^a	0.75 ^a	0.139(2)	0.7(2) ^c	1
O(9)	8b	0.375 ^a	0.25 ^a	0.143(2)	0.7(2) ^c	1
O(10)	8b	0.375 ^a	0.75 ^a	0.142(2)	0.7(2) ^c	1

Note. Space group $A2_1am$. $a = 10.7959(2)$ Å, $b = 5.4012(1)$ Å, and $c = 30.0755(6)$ Å. $R_p = 0.113$, $R_{wp} = 0.149$, $R_i = 0.077$. Constraints: for Cr(1) and O(4) $y = 2x$; $yO(2) = 2xO(1)$

^a Parameters not refined.

^{b,c} Parameters constrained to have the same values.

patterns (Fig. 4) show the validity of these refinements. On the basis of these refined positions, HREM images have been simulated. These calculations along $[100]$ and $[010]$ directions, for a defocus value close to -550 Å with a crystal thickness ranging to 30 to 80 Å, are inserted in Fig. 3. One observes that these simulated contrasts fit perfectly with the experimental images, especially the ordering phenomena between Sr and Cr species at the level of the intermediate $[AO]$ layer (white arrows in Fig. 3).

These results, although they cannot be considered as accurate about the oxygen positions coordinated to Cr(1), confirm without ambiguity the stacking sequence deduced from HREM observations. A structural model that shows the close relationships of this structure with the “0201–1201” intergrowth can be proposed (Fig. 5). One indeed recognizes $[Sr_2CrO_4]_{\infty}$ blocks, which exhibit a geometry similar to that of the “0201” structure of La_2CuO_4 , except that the pure octahedral layers are replaced by mixed octahedral–pyramidal layers. The fact that one CrO_6 octahedron out of two is replaced by one CrO_5 pyramid is due to the fact that the O(4) oxygen atom has moved away along \vec{c} . Despite the low accuracy of this oxygen position, the apical Cr(3)–O(4) distance of 3.09 Å must be considered as significant. The $[(Sr_{0.5}Cr_{0.5})Sr_2CrO_5]_{\infty}$ blocks are also closely related to the “1201” $[TlBa_2CuO_5]_{\infty}$ blocks previously observed for $TlBa_{2-x}La_{2+x}Cu_2O_9$ (17); nevertheless they differ fundamentally from the latter by the nature of the intermediate layer $[(Cr_{0.5}Sr_{0.5})O]_{\infty}$ compared with that of

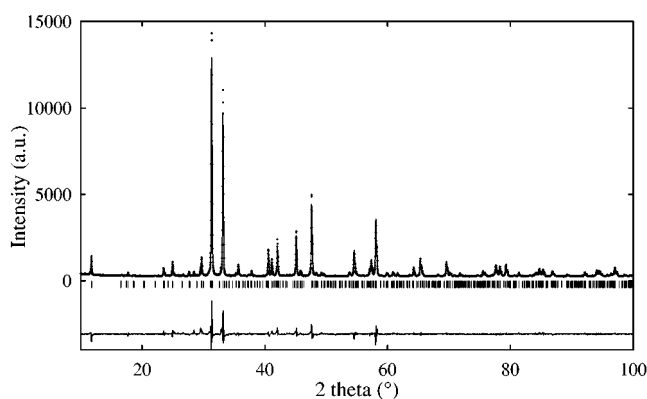


FIG. 4. Experimental (filled circle) and calculated (solid line) powder X-ray diffraction patterns of the $\text{Sr}_{4.5}\text{Cr}_{2.5}\text{O}_9$ phase. Vertical bars indicate the Bragg angle positions refined in the $A2_1am$ space group.

the $[\text{TlO}]_\infty$ layer. The O(1) and O(2) atoms are brought significantly closer to Cr(1), forming CrO_4 tetrahedra. As a consequence, the structure of $\text{Sr}_{4.5}\text{Cr}_{2.5}\text{O}_9$, although it derives from the “0201–1201” type structure, can also be described as the stacking along \vec{c} of three types of chromium polyhedra, tetrahedral in the $[(\text{Sr}_{0.5}\text{Cr}_{0.5})\text{O}]$ layers, and mixed octahedral–pyramidal in the pure $[\text{CrO}_2]$ layers, intergrown with $[\text{SrO}]$ -type layers.

As mentioned above, the atomic positions of oxygen atoms cannot be considered as accurate, especially those concerning O(1), O(2), and O(4); a neutron diffraction study

will be needed to better understand this structure in detail. Nevertheless the analysis of the Cr–O interatomic distances (Table 2) allows for some interesting features to be emphasized. The Cr(1) atom in tetrahedral coordination exhibits two short Cr–O distances (1.64 Å) that are compatible with the presence of Cr^{6+} ; however two other distances of 1.96 Å are abnormally long for Cr^{6+} and may result from erroneous positions of O(1) and O(2). The Cr(2)–O distances corresponding to the octahedral sites, ranging from 1.91 to 2.14 Å, suggest that this site is occupied by trivalent chromium. The pyramidal coordination of Cr(3) is quite unusual, though the five Cr–O distances are compatible with trivalent chromium. Such a coordination has only been reported, to our knowledge, in the layered oxysulfide $\text{Sr}_2\text{CuCrO}_3\text{S}$ (19) where chromium is also trivalent, the sixth nearest neighbor S being also located far away (3.20 Å). These observations suggest strongly that chromium exhibits in this phase a disproportionation, forming Cr(VI) tetrahedral $[(\text{Sr}_{0.5}\text{Cr}_{0.5})\text{O}]$ layers alternating with pure Cr(III) mixed octahedral–pyramidal layers. This hypothesis (20% of Cr^{6+} and 80% of Cr^{3+}) is consistent with the actual chemical composition, namely $\text{Sr}_{4.5}\text{Cr}_{2.5}\text{O}_{8.9}$, which leads to a formal valence state for chromium close to 3.5 while the investigation of the magnetic properties of this phase (see next section) strongly supports this viewpoint. However a fine structural analysis from neutron diffraction data will be necessary to clarify the actual oxygen content and their atomic positions and thus confirm the valence of different chromium species.

The other interatomic distances, namely Sr–O, ranging from 2.31 to 2.81 Å, are in agreement with those usually observed in chromium-based oxides (15, 20–22).

III. Magnetic Properties

The temperature dependence of the low-field dc susceptibility ($H = 0.1$ T) in the range 5 to 400 K (Fig. 6) shows a well-defined peak at $T_N \approx 125$ K, characteristic of the antiferromagnetic nature of the transition. However, below 100 K, a rise with a further decrease in temperature can be explained by the appearance of a weak spontaneous magnetic moment. It should be noted that the temperature transition is independent of frequency in ac susceptibility measurements between 10 Hz and 1 kHz. Figure 7 gives the reciprocal low-field dc susceptibility. As shown for temperatures above 300 K, χ_{dc}^{-1} obeys Curie–Weiss law of the type

$$\chi = \frac{N\mu_{\text{eff}}^2}{3k_B(T - \theta)} = \frac{C}{T - \theta}.$$

FIG. 5. Perspective view of the structure of the $\text{Sr}_{4.5}\text{Cr}_{2.5}\text{O}_9$ showing the Sr:Cr ordering and distorted chromium polyhedra along the (a) $[010]$ and (b) $[100]$ directions.

It results in a Curie constant of $C = 3.38 \text{ emu}\cdot\text{K}^{-1}\cdot\text{mol}^{-1}$ and a paramagnetic Curie temperature $\theta = -208$ K,

TABLE 2
Main Interatomic Distances and Angles

<i>M</i> -O	$\times n$	<i>d</i> (Å)	<i>M</i> -O	$\times n$	<i>d</i> (Å)	Selected angles	
Sr(1)-O(1)	2	2.754(8)	Cr(1)-O(1)	1	1.95(5)	O(1)-Cr(1)-O(2)	103(1)°
O(2)	2	2.754(8)	O(2)	1	1.95(2)	O(1)-Cr(1)-O(4)	108(2)°
O(3)	2	2.31(3)	O(4)	2	1.64(3)	O(2)-Cr(1)-O(4)	108(2)°
						O(4)-Cr(1)-O(4)	120(2)°
Sr(2)-O(1)	1	2.58(1)	Cr(2)-O(3)	1	2.03(3)		
O(3)	2	2.710(3)	O(5)	1	2.14(4)		
O(4)	1	2.62(4)	O(7)	1	1.911(2)		
O(7)	1	2.58(4)	O(8)	1	1.911(5)		
O(8)	1	2.73(4)	O(9)	1	1.911(2)		
O(9)	1	2.67(4)	O(10)	1	1.913(1)	Cr(2)-O(7)-Cr(3)	170°(2)
O(10)	1	2.45(3)				Cr(2)-O(8)-Cr(3)	178°(2)
						Cr(2)-O(9)-Cr(3)	177°(2)
Sr(3)-O(2)	1	2.591(8)	Cr(3)-O(4)	1	3.16(3)	Cr(2)-O(10)-Cr(3)	158°(2)
O(3)	2	2.711(3)	O(6)	1	1.71(3)		
O(4)	1	2.62(2)	O(7)	1	1.93(1)		
O(7)	1	2.58(4)	O(8)	1	1.911(2)		
O(8)	1	2.72(4)	O(9)	1	1.915(5)		
O(9)	1	2.67(4)	O(10)	1	1.97(1)		
O(10)	1	2.45(3)					
Sr(4)-O(5)	2	2.720(4)					
O(5)	1	2.39(3)					
O(6)	2	2.702(1)					
O(7)	1	2.70(5)					
O(8)	1	2.56(4)					
O(9)	1	2.61(4)					
O(10)	1	2.84(4)					
Sr(5)-O(5)	2	2.720(4)					
O(6)	2	2.702(1)					
O(6)	1	2.63(3)					
O(7)	1	2.69(5)					
O(8)	1	2.55(4)					
O(9)	1	2.60(4)					
O(10)	1	2.83(4)					

consistent with an antiferromagnetic phase transition. Considering the coexistence of nonmagnetic Cr⁶⁺ layers and magnetic Cr³⁺ layers, according to the structural results, an effective paramagnetic moment of 3.66 μ_B per magnetic species can be deduced from the $\chi^{-1}(T)$ curve, close to the typical experimental value 3.80 μ_B (see for instance Ref. (19)) expected for Cr³⁺. Thus, the magnetic measurements are compatible with the Cr⁶⁺/Cr³⁺ distribution deduced from the structural study that shows the coexistence of nonmagnetic Cr⁶⁺ and magnetic Cr³⁺ in the 1201 term of the intergrowth and only magnetic Cr³⁺ in the K₂NiF₄-type term. This implies that the magnetism in Sr_{4.5}Cr_{2.5}O₉ originates only from the Cr³⁺ ion sublattice. The structure can be described as magnetic K₂NiF₄-like double layers that are separated along \vec{c} axis by the nonmagnetic [SrO]-[Sr_{0.5}Cr_{0.5}O]-[SrO] layers.

According to the symmetric superexchange rules (23), it has been found that magnetic order in oxides showing K₂NiF₄-type structure corresponds to AF coupling within the planes (24, 25). Moreover, for simple reasons of symmetry, interactions between neighboring layers in the ordered state should be cancelled by the AF interactions within the planes, leading to a 2D magnetic behavior. According to our previous structural description, such a cancellation cannot occur in this intergrowth. Furthermore, our magnetic data show a sharp minimum in the reciprocal dc susceptibility, implying significant interplanar superexchange, i.e., 3D magnetic coupling at low temperature. Although a mean field model remains a rough approximation, a calculation of the nearest-neighbor exchange integral J/k_B (intraplane coupling) and of the second neighbor integral J'/k_B (interplane coupling) gives -12.5 K and -3.1 K,

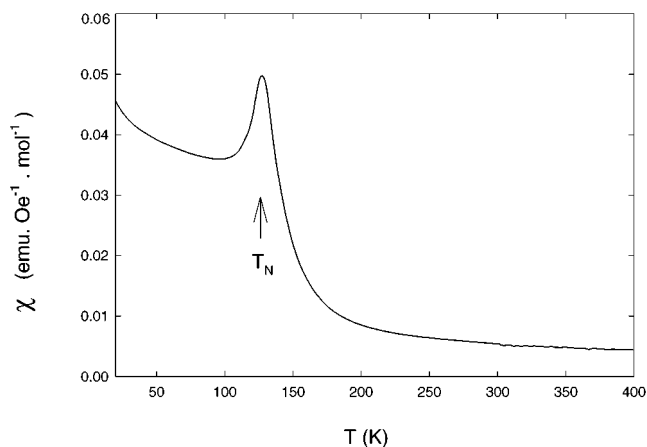


FIG. 6. Thermal dependence of the low-field dc susceptibility.

respectively. The obtained value of J is quite low compared to that reported previously in K_2NiF_4 -type compounds involving the same magnetic ions (24). Such a result is consistent with a nonnegligible interlayer coupling. It has indeed been shown for oxides that the transition from a 2D structure to a perovskite 3D decreases J/k_B . For instance, in the $\text{CaLa}_{1-x}\text{Y}_x\text{CrO}_4$ series related to a K_2NiF_4 -type structure, Berjoan *et al.* (25) have shown that the magnetic properties are mostly characterized by a 2D magnetic coupling due to the half-filled t_{2g} orbitals of Cr^{3+} . However, for $x = 1$, because of an increase of the covalency of apical Y–O bonds, a 3D-type interaction occurs. On the basis of the structural study performed on our $\text{Sr}_{4.5}\text{Cr}_{2.5}\text{O}_9$ phase and as emphasized by Leflem *et al.* (24), we believe that the 1201 term of the intergrowth acts in the same fashion by creating a distortion in the K_2NiF_4 -type term of the structure and, thus, by reducing the distance between magnetic Cr^{3+} in the blocks' K_2NiF_4 -like double layers.

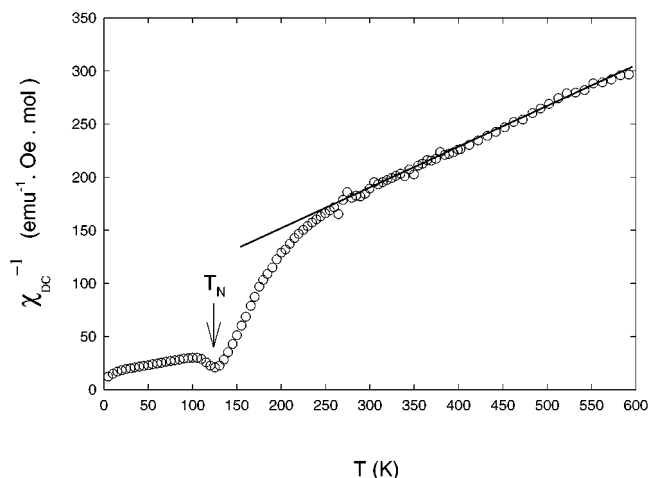


FIG. 7. Thermal dependence of the reciprocal low-field dc susceptibility. The solid line corresponds to Curie-Weiss extrapolation with parameters given in the text.

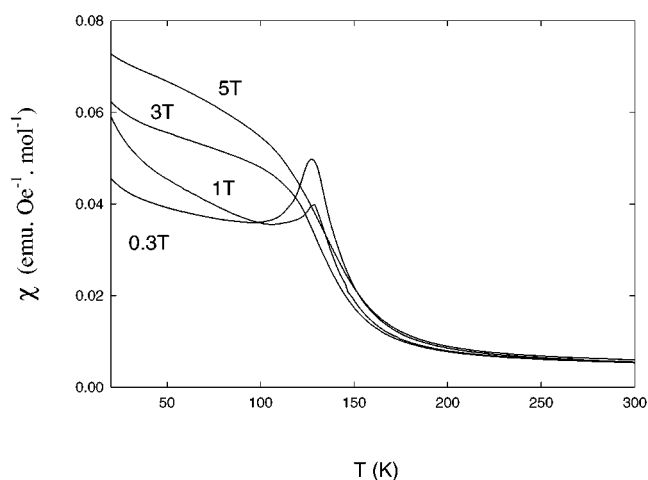


FIG. 8. Comparison of the $\chi(T) = (M/H)$ of $\text{Sr}_{4.5}\text{Cr}_{2.5}\text{O}_9$ for ZFC conditions in different fields.

In Fig. 8, χ_{dc} (ZFC mode) as a function of temperature for various values of the applied magnetic field, $H = 0.3$ T, 1 T, 3 T, and 5 T, is displayed. Note that χ_{dc} is significantly different; depending on the value of the magnetic field, the peak associated with the AF order becoming less defined as the field increases. For $H \geq 3$ T this peak is suppressed and a trend to saturation, reminiscent of a ferromagnet, is observed. To summarize, the peak due to the antiferromagnetic ordering of the Cr^{3+} moments disappears and is replaced by a response suggesting the presence of ferromagnetic correlation between the moments at low temperature. This field-induced transition is due to a metamagnetic behavior that is demonstrated in Fig. 9 where the magnetization as a function of the applied field is shown for temperature below and above the AF-ordering temperature, $T_N = 125$ K. For $T < T_N$, one can observe a significant deviation of magnetization from linearity at a critical field $H_c(T)$. The jump in the $M(H)$ curves is not abrupt but smooth, probably due to the fact that our sample is polycrystalline. The nature of the sample is also consistent with the nonprominent hysteresis effect observed at low temperature; as the temperature increases, this hysteresis in the $M(H)$ curves becomes smaller and is absent for $T = 50$ K. At $T = 5$ K, the magnetization reaches $0.34 \mu_B/\text{Cr}^{3+}$ for an applied field of 5 T. This value is far from the average spin of a single Cr^{3+} ion; hence chromium spins cannot be regarded as fully for a maximum applied field of 5 T. A plot of M vs H^{-1} (not shown) allows an extrapolated estimate for this saturation magnetization to be made and yields $0.43 \mu_B/\text{Cr}^{3+}$ at 5 K. This result is discussed in the following in terms of a partial spin-flop transition.

Figure 10 exhibits the differential magnetization dM/dH as a function of field for field-increasing process. The transition field is assigned by the inflection point of the

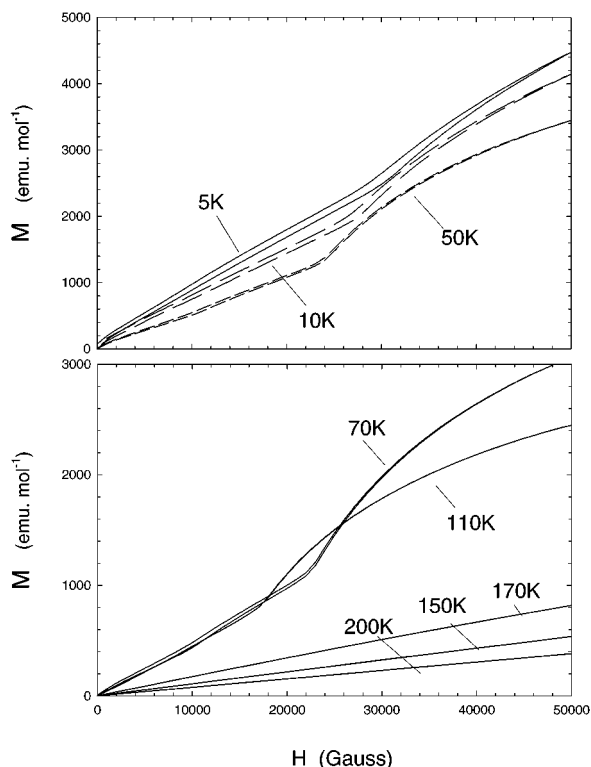


FIG. 9. Magnetization as a function of the applied field for various temperatures. The $M(H)$ curves show the features of metamagnetic transition.

$M(H)$ curve that corresponds to a bump in dM/dH vs H at each temperature (see arrows). It has been checked that the field-sweeping process hardly affects the value of the critical field $H_c(T)$. The obtained phase diagram is given in Fig. 11. The transition field decreases with increasing temperature and at temperatures above $T_N = 125$ K it cannot be defined.

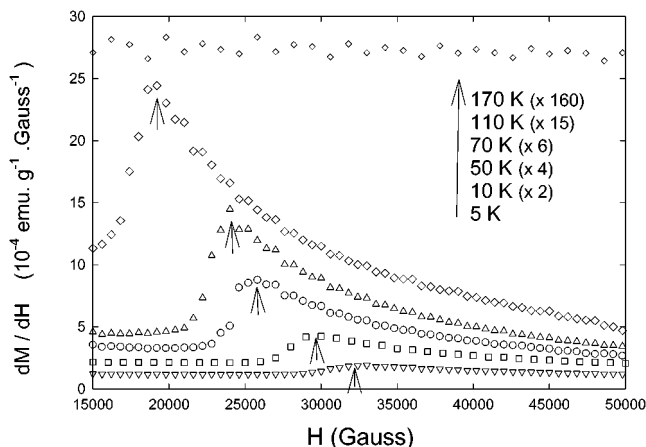


FIG. 10. Differential susceptibility as a function of the applied field. The data for $T = 5, 10, 50, 70, 110, 170$ K have been offset for clarity. The transition fields are assigned by arrows.

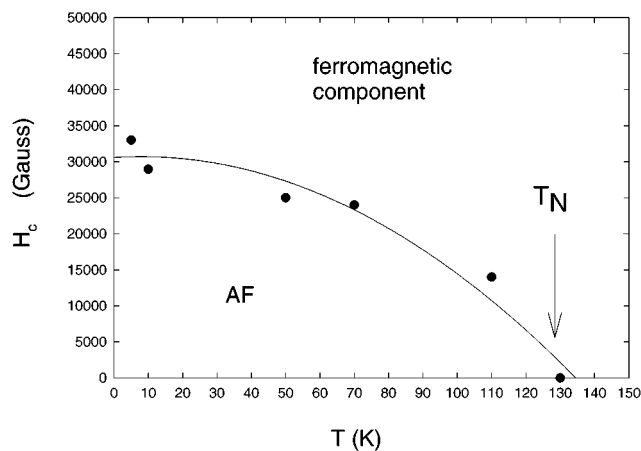


FIG. 11. Phase diagram of $\text{Sr}_{4.5}\text{Cr}_{2.5}\text{O}_9$ in the H - T plane.

This demonstrates that the metamagnetic transition takes place only below T_N .

Such a metamagnetic behavior can be found in numerous AF-ordered materials (26–28). This is the case of La_2CuO_4 (29, 30), which presents a K_2NiF_4 -type structure and is considered as a good approximation of a 2D Heisenberg antiferromagnet. Ting *et al.* (29) and later Tineke *et al.* (30) have explained the hidden ferromagnetic and metamagnetic behaviors of low-field dc susceptibility including a Dzyaloshinskii–Moriya (DM) antisymmetric superexchange term (31) in the spin Hamiltonian of the system. Concerning our phase and backing up our assertions with the results obtained through the previous structural study, we believe that the metamagnetism may arise from an antisymmetric intralayer coupling. As shown in the previous section, application of the Goodenough’s rules in the chromium layer of the double K_2NiF_4 -like layer blocks leads us to expect intraplanar AF coupling in agreement with the calculated value of the exchange integral ($J = -12.5$ K). Moreover, the slight 3D magnetic behavior detected in the susceptibility behavior implies a weak AF interlayer coupling ($J' = -3.1$ K). The structural study has evidenced the fact that the symmetry of the blocks’ K_2NiF_4 -like double layers of the intergrowth is disturbed because of the alternation of a square–pyramidal coordination geometry and of a classical octahedral geometry of the Cr^{3+} cations with periodicity 1:1. This peculiarity induces a non $-180^\circ\text{Cr}^{3+}-\text{O}-\text{Cr}^{3+}$ bonding within the layers in agreement with experimental angles (Table 2). We believe that this may lead to an antisymmetric superexchange interaction between chromium atoms that could produce a canting of the spin away from the antiparallel configuration and induce a ferromagnetic component. However, the weak interplane AF interactions can be destroyed by a finite applied field that allows these ferromagnetic moments to be developed. Therefore, a jump in the magnetization vs temperature can occur, in

good agreement with our experimental data. Moreover, the very small value of the extrapolated magnetization at saturation for 5 K is consistent with the extremely small ferromagnetic component induced by such a behavior.

CONCLUDING REMARKS

This work evidences the possibility of generating in the ternary Sr–Cr–O system a new chromium-based layered oxide family related to a regular intergrowth between 1201- and K_2NiF_4 -type structures. The main structural features of the $\text{Sr}_{4.5}\text{Cr}_{2.5}\text{O}_9$ phase concern the 1:1 Sr–Cr ordering within the intermediate layer of the 1201-type block and the coexisting of three chromium polyhedra. However a complementary neutron study will be necessary to define the fine crystal structure. This new layered oxide exhibits simultaneously a complex structure and an original metamagnetic transition which open new investigation ways, especially the stabilization of new chromium-based layered oxides with interesting magnetic properties.

ACKNOWLEDGMENTS

The authors are grateful to Dr. N. Nguyen for susceptibility data at high temperature and Professors M. Hervieu and V. Caignaert for many helpful discussions.

REFERENCES

1. R. S. Ruddlesden and P. Popper, *Acta Crystallogr.* **10**, 538 (1957); *ibid.* **54**, 11 (1958).
2. B. Raveau, C. Michel, M. Hervieu, and D. Groult, "Crystal Chemistry of High T_c Superconducting Copper Oxides," Springer-Verlag Series. Springer-Verlag, Berlin, 1991.
3. M. Imada, A. Fujimori, and V. Tokura, *Rev. Mod. Phys.* **70**, 1039 (1999). [See also "Colossal Magnetoresistance, Charge Ordering and Related Properties of Manganese Oxides." C. N. R. Rao and B. Raveau, (Eds.), World Scientific, Singapore, 1998.]
4. V. Caignaert, Ph. Daniel, N. Nguyen, A. Ducouret, D. Groult, and B. Raveau, *J. Solid State Chem.* **112**, 126 (1994).
5. Ph. Daniel, L. Barbey, D. Groult, N. Nguyen, G. Van Tendeloo, and B. Raveau, *Eur. J. Solid State Inorg. Chem.* **31**, 235 (1994); *J. Phys. Chem. Solids* **55**, 795 (1994); *Mater. Chem. Phys.* **45**, 33 (1996).
6. T. Seguelm, P. Maestro, J. C. Grenier, L. Fournes, and M. Pinchard, *Physica B* **215**, 427 (1995).
7. Ph. Boullay, B. Domengès, D. Groult, and B. Raveau, *J. Solid State Chem.* **124**, 1 (1996).
8. D. Groult, C. Martin, A. Maignan, D. Pelloquin, and B. Raveau, *Solid State Commun.* **105**, 583 (1998).
9. J. M. Tarascon, P. F. Miceli, P. Barboux, D. M. Hwang, G. W. Hull, M. Giroud, L. H. Green, Y. Lepage, W. R. Mc Kinnon, E. Tselepis, G. Pleizier, M. Eibschultz, D. A. Neumann, and J. J. Phyne, *Phys. Rev. B* **39**, 11,587 (1989).
10. D. Pelloquin, A. C. Masset, A. Maignan, M. Hervieu, C. Michel, and B. Raveau, *J. Solid State Chem.* **148**, 108 (1999).
11. S. Naray-Szabo, *Naturwissenschaften* **31**, 466 (1943).
12. A. Daoudi and G. Le Flem, *Mater. Res. Bull.* **8**, 1103 (1973).
13. R. Berjoan, J. P. Coutures, G. Le Flem, and M. Saux, *J. Solid State Chem.* **42**, 75 (1982).
14. C. Chaumont, G. Le Flem, and P. Hagenmuller, *Z. Anorg. Allg. Chem.* **470**, 18 (1980).
15. K. A. Wilhelm, *Arkiv Kemi* **26**, 157 (1967).
16. O. Glenser, U. Hauschild, F. Truepel, *Z. Anorg. Allg. Chem.* **277**, 113 (1954).
17. C. Martin, A. Maignan, M. Huvé, M. Hervieu, C. Michel, and B. Raveau, *Physica C* **179**, 1 (1991).
18. J. Rodriguez-Carvajal, *Physica B* **192**, 55 (1993).
19. W. J. Zhu and P. H. Hor, *J. Solid State Chem.* **134**, 128 (1997).
20. H. Pausch and Hk Müller-Buschbaum, *Z. Anorg. Allg. Chem.* **405**, 1 (1974).
21. E. Cuno and Hk Müller-Buschbaum, *Z. Anorg. Allg. Chem.* **572**, 95 (1989).
22. E. Cuno and Hk Müller-Buschbaum, *Z. Anorg. Allg. Chem.* **572**, 175 (1989).
23. J. B. Goodenough, *Phys. Rev.* **100**, 564 (1955).
24. G. Leflem, Ph. Courbin, C. Delmas, and J. L. Soubeyroux, *Z. Anorg. Allg. Chem.* **476**, 69 (1981).
25. R. Berjoan, J. P. Coutures, G. Leflem, and M. Saux, *J. Solid State Chem.* **42**, 75 (1982).
26. H. P. Kunkel, X. Z. Zhou, P. A. Stampe, J. A. Cowen, and G. William, *Phys. Rev. B* **53**, 15,099 (1996).
27. C. Mazumdar, A. K. Nigam, R. Nagarajan, L. C. Gupta, C. Godar, B. D. Godart, and B. D. Padalia, *Phys. Rev. B* **54**, 6069 (1996).
28. V. K. Pecharsky, K. A. Gschneider, and L. L. Miller, *Phys. Rev. B* **43**, 10,906 (1991).
29. S. T. Ting, P. Pernambuco-Wise, J. E. Crow, E. Manousakis, and J. Weaver, *Phys. Rev. B* **46**, 11,772 (1992).
30. T. Tineke, T. R. Thurston, and N. W. Preyer, *Phys. Rev. B* **38**, 905 (1988).
31. I. E. Dzyaloshinskii, *J. Phys. Chem. Solids* **4**, 241 (1958); Moriya, *Phys. Rev.* **120**, 91 (1960).